LETTER | OCTOBER 01 2025

Global properties and stability of transonic plasma acceleration in the magnetic nozzle

N. Sheth ; A. Smolyakov ; J. Deguire ; S. Pande ; P. N. Yushmanov

Phys. Plasmas 32, 100701 (2025)
https://doi.org/10.1063/5.0286532

Physics of Plasmas LETTER pubs.aip.org/aip/pop

Global properties and stability of transonic plasma acceleration in the magnetic nozzle

Cite as: Phys. Plasmas **32**, 100701 (2025); doi: 10.1063/5.0286532
Submitted: 19 June 2025 · Accepted: 15 September 2025 ·
Published Online: 1 October 2025

N. Sheth,[1,a)] A. Smolyakov,[1] J. Deguire,[1] S. Pande,[2] and P. N. Yushmanov[3]

AFFILIATIONS

[1]Department of Physics and Engineering Physics, University of Saskatchewan, Saskatoon SK S7N 5E2, Canada
[2]Indian Institute of Technology (BHU), Varanasi, India
[3]TAE Technologies Inc., 19631 Pauling, Foothill Ranch, California 92610, USA

[a)]Author to whom correspondence should be addressed: nishka.sheth@usask.ca

ABSTRACT

It is shown that transonic plasma acceleration in the converging–diverging magnetic field (magnetic nozzle) follows the unique global solution which is fully defined by the magnetic field. Such solution, which was analytically obtained earlier in the paraxial approximation, is compared here with the results of the axisymmetric two-dimensional ($r - z$) magnetohydrodynamics simulations. It is shown that the analytical solution not only describes well the region near the axis but also can be applied to arbitrary magnetic surfaces. The simulations with different length of the nozzle and different boundary values for plasma velocity show that the plasma flow switches to the unique transonic acceleration profile via the shock-like transition in the velocity and pressure profiles. The simulations with arbitrary (not vacuum) initial magnetic field demonstrate the global adjustment of the magnetic field such that the transonic acceleration velocity profile follows the analytic predictions with the modified magnetic field.

Expanding magnetic field (magnetic nozzle) and converging–diverging (magnetic mirrors) configurations are of interest for electric propulsion,[1–3] material processing and advanced manufacturing,[4] and fusion[5,6] applications. Magnetic mirrors, with converging–diverging magnetic field configurations, are used to confine plasma in fusion devices.

Plasma acceleration in the magnetic nozzle was demonstrated in early experiments.[7,8] Transonic plasma acceleration guided by the magnetic field is a basis of electrodeless plasma thrusters for space propulsion[2,9] and also considered in plasma sources for advanced material processing.[4] Plasma expansion in the diverging magnetic field is a crucial process in a divertor of the open mirror systems,[5,10] which are used to accept and direct large energy fluxes to the material walls. Plasma flow guided and controlled by the magnetic field is a key question for these applications.

General equilibrium equations for steady-state flows were formulated within one- and two-fluid magnetohydrodynamics (MHD),[11,12] in particular, for applications to the problem of equilibrium and stability of fusion plasmas.[13,14] Similar physics is involved in the problem of plasma flows in space,[15] solar wind acceleration[16] and astrophysical winds and jets.[17] In general, these models generalize the Grad–Shafranov equilibrium problem to include the inertial forces into the equilibrium.

The balance of the inertial force with the electric field (or pressure) force is the main element of the acceleration and equilibrium in the magnetic nozzle. In the context of propulsion applications, a simple model of transonic plasma acceleration can be formulated in the quasi-two-dimensional (2D) (paraxial) approximation, which is effectively reduced to the 1D problem.[18–21]

The acceleration of cold ions is governed by the stationary parallel momentum balance

$$m_i V_\parallel \nabla_\parallel V_\parallel = eE_\parallel, \tag{1}$$

where the parallel electric field $E_\parallel$ is maintained by the electron pressure gradient of expanding plasma

$$-enE_\parallel - \nabla_\parallel p_e = 0, \tag{2}$$

and the plasma density variation is controlled by the continuity equation

$$\nabla_\parallel (nV_\parallel / B) = 0. \tag{3}$$

Here, $\nabla_\parallel = \mathbf{B}\cdot\nabla/B$ is the gradient along the magnetic field, and $V_\parallel$ and $E_\parallel$ are, respectively, the ion velocity and the electric field along the magnetic.

In the paraxial approximation, the inverse magnetic field $B(z)$ in Eq. (3) plays the role of the flux tube cross section, $A \sim 1/B(z)$, and Eqs. (1)–(3) become one-dimensional equations along the z-direction. For isothermal electrons with $T_e = const$, $p_e = nT_e$, from Eqs. (1)–(3), one can obtain the expression for the normalized ion velocity $M = V_\parallel/C_s$ in the form[21]

$$\frac{M^2}{2} = \ln\left(\exp(c_m) M \frac{B_m}{B(z)}\right), \tag{4}$$

where C_s is the ion-sound speed, $B = B(z)$ is the magnetic field as a function of the distance along the nozzle (near the axis ($r/a \ll 1$), and B_m is the maximum value of the magnetic field. The value of the c_m constant defines the particular solution. An example of the solutions diagram for the converging–diverging magnetic field used in this paper is shown in Fig. 1. An exact solution of Eq. (4) can be written[21] in terms of the Lambert function $W(y)$ defined as the solution of the equation $W\exp(W) = y$.

$$M(z) = \left[-W\left[-b^2(z)\exp(-2c_m)\right]\right]^{1/2}, \tag{5}$$

where $b(z) = B(z)/B_m$.

The plasma velocity along the transonic solution with $c_m = 0.5$ is fully defined by the regularization condition at the magnetic throat, i.e., by the condition that the plasma flow $V_\parallel$ is equal to the sound velocity C_s at the location of the maximum magnetic field, thus removing the singularity at $V_\parallel = C_s$.[21] Such regular solutions follow the magnetic field profile as expressed by Eq. (5). This is a single unique transonic accelerating solution represented by the separatrix in Fig. 4. The other separatrix, representing a decelerating solution, may be of interest for accreting objects in astrophysics or potentially for direct recuperation of the kinetic plasma energy into electricity, but is not considered here. The subsonic part, $M < 1$, of the transonic accelerating solution is described by $M = [-W_0(-b^2(z)/e)]^{1/2}$ branch of the Lambert function, and the supersonic is given by the other branch $M = [-W_{-1}(-b^2(z)/e)]^{1/2}$, where e is Euler's number. The full

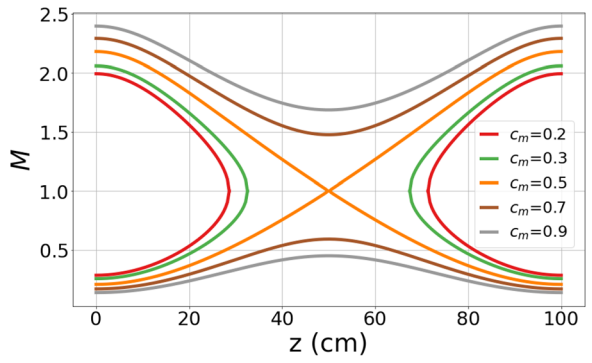

FIG. 1. A typical diagram of the solutions for plasma flow in converging–diverging magnetic nozzle given by Eq. (4). The $c_m < 0.5$ curves define the subsonic profiles, $c_m > 0.5$ define supersonic profiles. The accelerating transonic profile is given by the separatrix with $c_m = 0.5$.

accelerating solution is formed by two branches $W_0(y)$ and $W_{-1}(y)$, which match smoothly[22,23] at the point $M = 1$ corresponding to the maximum magnetic field B_m.

For the converging–diverging magnetic nozzle with the maximum magnetic field B_m at the throat, all possible solutions in Fig. 4 can be separated into several groups and can be classified by the value of the velocity at the nozzle inlet, $z = 0$. At the nozzle inlet, the transonic solution has $M(0) = [-W_0(-(B(0)/B_m)^2/e)]^{1/2}$, and at the nozzle end $M(L) = [-W_{-1}(-(B(L)/B_m)^2/e)]^{1/2}$. The solutions with $V_\parallel/C_s < M(0)$ remain purely subsonic, and for $V_\parallel/C_s > [-W_{-1}(-(B(0)/B_m)^2/e)]^{1/2}$ remain purely supersonic in the whole region. The solutions with the boundary values (at $z = 0$) between two separatrices $[-W_0(-(B(0)/B_m)^2/e)]^{1/2} < V_\parallel/C_s < [-W_{-1}(-(B(0)/B_m)^2/e)]^{1/2}$ are multi-valued and not physical. The analytical solution in Eq. (5) was obtained in the simplified (effectively 1D) case corresponding to the paraxial limit. It was found that such solutions are robust as they were realized in drift-kinetic and fluid simulations within similar 1D paraxial models, i.e., plasma flow converges to the analytical transonic solutions for a rather wide range of initial conditions.[24–26] It is relatively straightforward to show theoretically that the model in Ref. 21 can be reformulated in terms of the 1D problem along the arbitrary magnetic field surfaces, with the length along the magnetic field line as the longitudinal coordinate. The goal of this article is to investigate plasma acceleration in a full 2D axisymmetric $(r-z)$ geometry and compare it with the analytical predictions. We demonstrate here that the theoretical solution in Eq. (5) remains valid when applied along the magnetic surfaces. The robust behavior of the transonic acceleration in the 2D MHD model was shown preliminarily in Ref. 27.

We employ here the standard ideal one-fluid MHD. The standard continuity, momentum, and magnetic field evolution equations of the ideal one-fluid MHD in the conservative form are

$$\frac{\partial\rho}{\partial t} + \nabla\cdot(\rho\mathbf{V}) = 0, \tag{6a}$$

$$\frac{\partial(\rho\mathbf{V})}{\partial t} + \nabla\cdot(\rho\mathbf{V}\mathbf{V} - \mathbf{B}\mathbf{B} + p_T\mathbf{I}) = 0, \tag{6b}$$

$$\frac{\partial\mathbf{B}}{\partial t} + \nabla\cdot(\mathbf{V}\mathbf{B} - \mathbf{B}\mathbf{V}) = 0, \tag{6c}$$

where the total plasma pressure is defined as $p_T = p + \frac{B^2}{2}$. In general, the equations for plasma density $\rho = m_i n$, velocity $\mathbf{V}$, and magnetic field $\mathbf{B}$ are supplemented by the equation of state that defines the thermal plasma pressure, which, in general, in various fusion and propulsion scenarios, can be anisotropic. It is often characterized by the isotropic equation of state with some effective value of the polytropic constant γ. The effects of varied γ on acceleration were studied in Ref. 21. Since it is not essential for the results of this paper, for simplicity, and to make the connection to the cold ions model in Eqs. (1)–(3), we use the isothermal model with constant temperature $T = T_e$ so that $p = nT_e$, and Eq. (6) forms a complete system.

One can show that in the stationary state, the axisymmetric plasma flow in one-fluid MHD exactly follows the magnetic field surface[11,13] as also assumed in the paraxial model.[21] In Eqs. (1)–(3), the gradient operator $\nabla_\parallel$ is the total derivative along the magnetic field. Thus, it is easy to see that in the stationary case $\partial/\partial t = 0$, Eq. (3) is

identical to Eq. (6a), and, after the exclusion of the electric field, Eqs. (1) and (2) reduce to the parallel (along $\mathbf{B}$) component of Eq. (6b). Thus, with respect to the stationary paraxial model in Eqs. (1)–(3), the MHD model introduces the general time dependence of all variables and two-dimensional effects.

As it is shown below, the most important result of this Letter is that the general time evolution of the system of Eq. (6) leads to self-consistent formation of the stationary transonic acceleration state with the velocity profile following the analytical predictions[21] from Eq. (5).

In our base case, we initialize simulations from a vacuum force-free magnetic field $\mathbf{B}_0$ defined by the poloidal flux function ψ in the form[28]

$$\mathbf{B}_0 = \frac{1}{r}\left(-\frac{\partial\psi}{\partial z}, 0, \frac{\partial\psi}{\partial r}\right), \tag{7}$$

with

$$\psi = \frac{r^2 B_*}{2}\left(1 - \frac{\alpha L}{\pi r}\cos\left(\frac{2\pi z}{L}\right) I_1\left(\frac{2\pi r}{L}\right)\right), \tag{8}$$

giving the magnetic field in the form

$$B_r = -B_*\alpha \sin\left(\frac{2\pi z}{L}\right) I_1\left(\frac{2\pi r}{L}\right), \tag{9}$$

$$B_z = B_*\left(1 - \alpha\cos\left(\frac{2\pi z}{L}\right) I_0\left(\frac{2\pi r}{L}\right)\right). \tag{10}$$

For the symmetric nozzle, $0 < z < L$, the resulting mirror ratio R, and the expansion ratio K are equal $R = K = (1+\alpha)/(1-\alpha)$, where $R = B_m/B(0)$, $K = B_m/B(L)$, and $B_m = B_*(1+\alpha)$. We have taken here the value of $B_* = 10^4$ G and $\alpha = 0.5$, resulting in $R = K = 3.0$. The functions I_0 and I_1 are modified Bessel functions of the first kind of order 0 and 1, respectively.

The ideal MHD Eq. (6) is solved in the 2D cylindrical $r-z$ geometry using the Godunov-type open source MHD code PLUTO v4.3.[29] The cylindrical nozzle domain of radius $a = 20$ cm and the axial length $L = 100$ cm is uniformly divided into 156×256 grid points. We chose the van Leer slope limiter, HLL Riemann solver, parabolic reconstruction scheme, and RK3 time-stepping with the Courant number 0.5.

In general, the magnetic field is evolving in time. For the base case, with the initial force-free field, the total magnetic field $\mathbf{B}$ is decomposed into a time-independent background component $\mathbf{B_0}$, given by Eq. (7), and a perturbation $\mathbf{B_1}$, such that $\mathbf{B} = \mathbf{B_0} + \mathbf{B_1}$. The magnetic field in the form of Eq. (7) inherently satisfies the solenoidal condition and is curl-free. The background magnetic field, $\mathbf{B_0}$, is held constant at all boundaries, while the perturbations of $\mathbf{B_1}$ remain free to evolve. This enables the Background Splitting option in the PLUTO code. The divergence-free condition on the $\mathbf{B_1}$ is maintained through the application of the constrained transport algorithm.

We initialize computations from the stationary plasma state with $\mathbf{V} = 0$ and uniform density ρ_0. At the axis of symmetry, $r = 0$, an axisymmetric condition is enforced; the outer radial boundary at $r = a$ fixes the ρ and $\mathbf{V}$ to their initial values. At the nozzle inlet, $z = 0$, the values of plasma density and axial velocity (V_z) are maintained as boundary conditions:

$$\rho = 4m_H n_0 \mathrm{sech}^2\left(\kappa^2\left(\frac{r}{a}\right)^2\right) + \rho_0, \tag{11}$$

$$V_z = v_0 C_s \mathrm{sech}^2\left(\kappa^2\left(\frac{r}{a}\right)^2\right). \tag{12}$$

Here, the parameter a represents the radial size of the simulation's domain, v_0 is a constant and its chosen values are defined for each figure below, and κ is an auxiliary parameter characterizing the peakness of the radial profile of the plasma source, so that overall, the a/κ gives the characteristic radius of the plasma injection profile, where we take $\kappa = 2.6$. At the exit of the nozzle, $z = L$, the outflow condition is imposed.

We use dimensional parameters $\rho_0 = 0.2 m_H n_0$ g/cm^3, with $n_0 = 10^{12}$ cm^{-3} and m_H is hydrogen mass. Here, the sound speed was $C_s = \sqrt{p/\rho} = \sqrt{k_B T/m_H}$ for the chosen temperature $T = 300$ eV. In this paper, we express time in the units of Alfvén time, denoted as $\tau_A = L/V_A$. Here, V_A refers to the Alfvén velocity, which is defined as $V_A = B_m/\sqrt{4\pi m_H n_0}$. Additionally, in what follows, the density is normalized by $\rho_m = 4m_H n_0 + \rho_0$.

The stationary flow equilibrium is established over the characteristic ion sound time $\tau_s = L/C_s$, which is much longer compared to the Alfvén time due to low plasma pressure $\beta = \tau_s^2/\tau_A^2 \ll 1$ for our parameters. The time evolution of the axial plasma density toward the equilibrium is shown in Fig. 2(a), and the final stationary state is established after several hundred τ_A. The radial density distribution essentially follows the boundary condition profile as demonstrated by Fig. 2(b), which shows the radial density profile at the different z locations. The 2D profiles of the plasma velocity and density in the stationary state, as shown in Figs. 3(a) and 3(b), demonstrate supersonic acceleration with the sonic point $V_\parallel = C_s$ at the location of the maximum magnetic field (nozzle throat). The time evolution of these

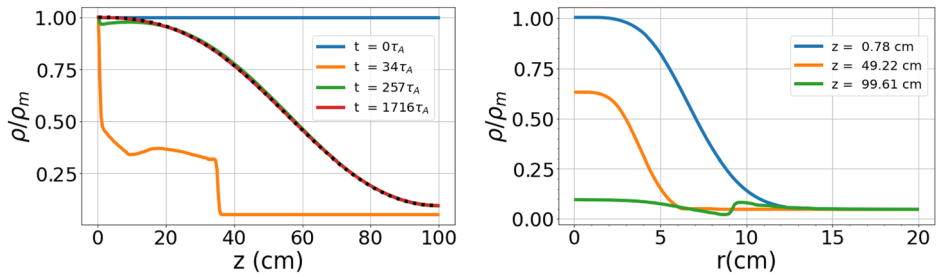

FIG. 2. (a) Time evolution of the plasma density toward the stationary state. The axial profiles of the density are shown at different times as labeled. The theoretical profile from Eq. (5) and mass conservation is shown by the dotted line. (b) The radial profiles of the density in the stationary state are shown at different locations in z as labeled.

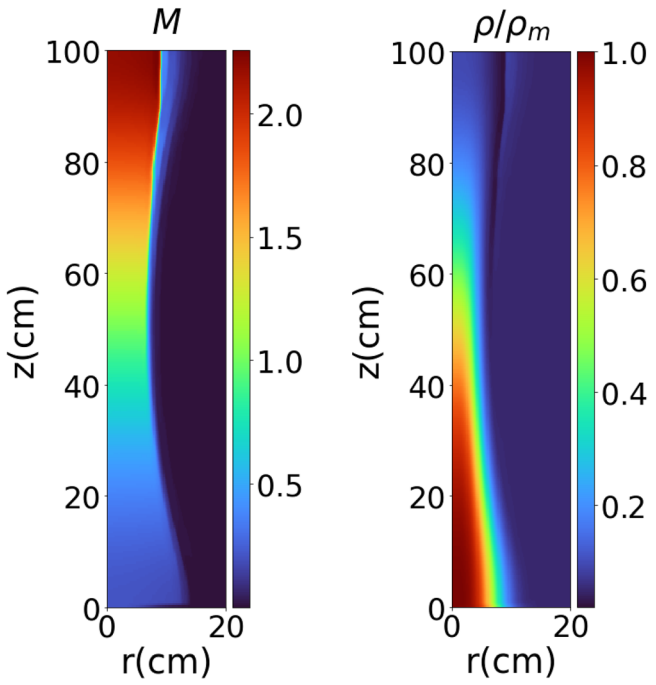

FIG. 3. Two-dimensional profiles of (a) plasma velocity and (b) density demonstrating the transonic acceleration. The sonic point transition, $M = 1$ occurs at the magnetic throat (maximum magnetic field) located at $z = 50$ cm.

profiles, highlighting the dynamic transition to the stationary state, is shown in the supplementary material.

We find an excellent agreement of the actual velocity profile (as a function of z near the axis $r = 0$) obtained in simulations with the analytical result of Eq. (5) as shown in Fig. 4. For this comparison, we have used the magnetic field as determined by Eqs. (7)–(10).

Our simulations demonstrate a remarkable stability of the transonic acceleration profile with respect to the variations in the boundary conditions. This is shown in the inset of Fig. 5, the stationary solution quickly transits into the unique transonic profile defined by Eq. (5), even when the boundary value of the axial velocity at the inlet $z = 0$ is

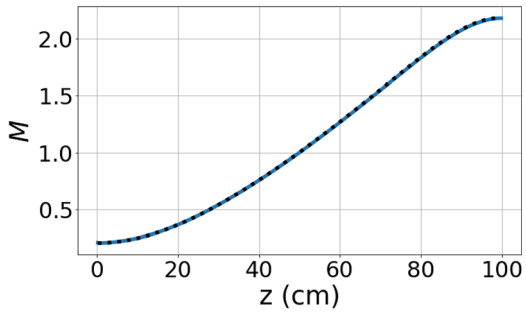

FIG. 4. The comparison of the stationary velocity profile obtained in simulations as a function of z, for $r = 0$ and $t = 1716\tau_A$, which is shown by the solid line, with the analytical solution given by Eq. (5), shown by the dotted line.

arbitrarily changed from its unique value of $V_z = 0.21C_s$ found from Eq. (5) for a given magnetic field.

This property is further illustrated by the results in Fig. 6(a), which shows several examples of the injection into the nozzle with different lengths and with different boundary values of the axial velocity. Thus, plasma injection with the boundary values of the velocity in the forbidden zone, between two separatrices in Fig. 1, with the $V_z = 0.4C_s$ also shown in Fig. 5, results in the transonic acceleration. We recall from Fig. 1 that in the supersonic (and subsonic) zone, there are multiple supersonic (and subsonic) solutions with different boundary values. However, the injection with the velocity in the subsonic zone does not produce fully subsonic flows as in Fig. 1. Such boundary conditions result in the transonic acceleration, as shown in Fig. 5 for the nozzle 0–100 cm and $V_z = 0.01C_s$ at $z = 0$, and in Fig. 6(a) for the nozzle 50–100 cm and with $V_z = 0.5C_s$ at $z = 50$ cm. This suggests that the subsonic solutions are unstable. On the contrary, the supersonic solutions are stable as shown in Fig. 6(a) for two examples: for the 20–100 cm nozzle with the boundary value of $V_z = 2.3C_s$ at $z = 20$ cm, and for the expanding nozzle of 50–100 cm and the injection value of $V_z = 4C_s$ at $z = 50$ cm. Figure 6(b) shows the behavior of the pressure profiles, which are consistent with the corresponding cases in Fig. 6(a).

The above examples show that the unique transonic profile, given by the analytical solution, is robustly valid near the axis $r = 0$, i.e., in the paraxial approximation as it was initially derived in Ref. 21.

In this paper, we show furthermore that the unique transonic solution remains valid when applied along the arbitrary magnetic

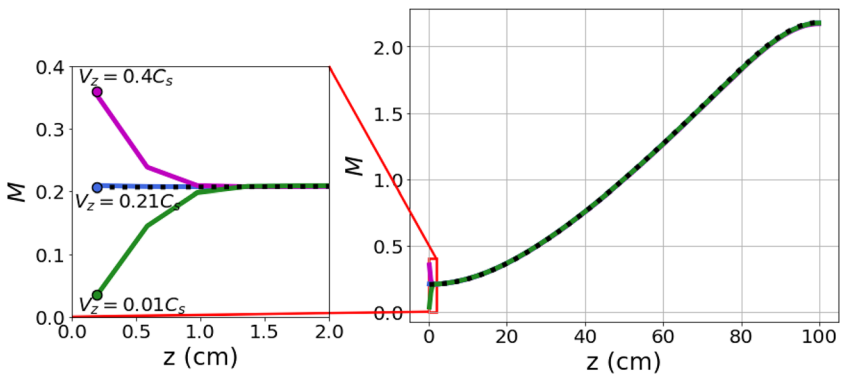

FIG. 5. Transonic acceleration velocity profiles, $M = V_{||}/C_s$, as a function of z for different boundary values of V_z at $z = 0$; the solid lines are from the simulations and the black dotted lines is for the theoretical solution from Eq. (5). The unique value of the velocity as predicted by Eq. (5) at $z = 0$ is $V_z = 0.21C_s$. The inset shows the behavior near $z = 0$, where the transition to the unique profile occurs over few grid cells.

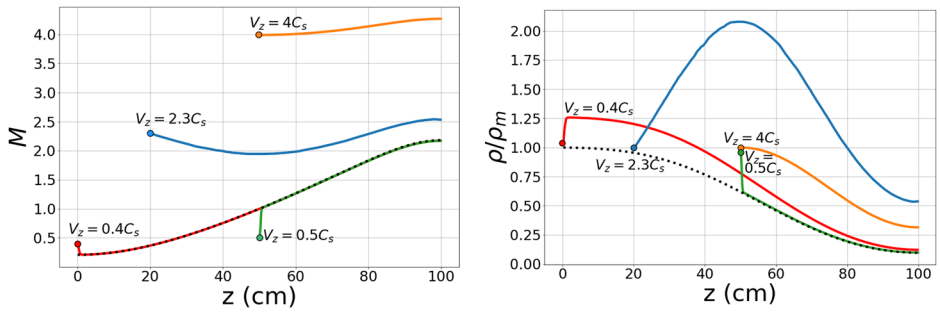

FIG. 6. Comparison of the theoretical and numerical results for (a) plasma velocity and (b) density for different nozzle lengths and different injection velocities. The black dotted lines are from the theoretical solution from Eq. (5) for the 0–100 cm domain. The solid lines are the numerical results: red for the 0–100 cm domain; blue for 20–100 cm domain; and green and orange for 50–100 cm domain. The boundary values of the injection velocity at the left are as labeled; the boundary values for the pressure are the same in all cases.

surface. The results in Figs. 5 and 6(a) show that independently of the boundary condition at the beginning of the nozzle, the stationary solution converges to the analytical solution in Eq. (5) (except for a narrow transition region in the beginning). Thus, at any location far from the transition region, the velocity can be found from Eq. (5) using the local value of the magnetic field. This has been tested in Fig. 7, which shows the stationary profiles of the velocity as a function of the radius at three different axial locations: $z = 0$, $z = 50$ cm, and $z = 100$ cm. The dotted lines show the values of the theoretical plasma velocity calculated from Eq. (5) for each location showing excellent agreement with the velocities obtained in simulations (solid lines) for finite values of r far from the axis. In this figure, we choose to show the radial dependence under constant z; any other line in the (r–z) plane will show the same property.

Our simulations well reproduce stationary analytical solutions in the bulk of the plasma jet. At the edge of the plasma column, we observe time-dependent fluctuations at the ion-sound timescale, these are seen in Figs. 2(b) and 7. Such fluctuations, also visible in the attached videos, are not described by our stationary model and result in deviations from the stationary momentum balance as shown in Fig. 10(a).

The above examples used the initial magnetic field from Eq. (8), which was a vacuum force-free field. We find that in the case of the initial vacuum field [Eq. (8)], the modification of the magnetic field is small but finite: just enough to balance small radial pressure gradient terms in the momentum balance. To further explore the properties of the unique transonic acceleration, we have also performed initial value simulations starting from different magnetic field given by the following model:

$$\psi = \frac{r^2}{2}\frac{B_m}{\left[1 + (R-1)((z-z_0)/L)^2\right]^{3/2}}, \tag{13}$$

where we choose R = 20.

In this case, one cannot use the background field option of PLUTO, but the other simulation parameters and settings, including the initial and boundary conditions, remain the same as in the base case, with the field from Eq. (8). The boundary conditions for the magnetic field at the radial boundary $r = a$ were imposed by fixing the values in the guard cells to the value of the initial magnetic field.

Similarly to the previous case, we observe the formation of the stationary transonic acceleration. This solution is shown by the solid orange line in Fig. 8. In this case, the numerical solution does not agree with the analytical solution obtained from Eq. (5) using the original magnetic field from Eq. (13), shown by the green dotted line and labeled as $t = 0$. However, the discrepancy disappears when the modification of the initial magnetic field in the course of the evolution is taken into account. These modifications are shown in

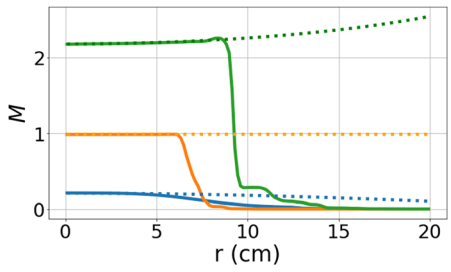

FIG. 7. Velocity profile, M, as a function of the radius at $z = 0$ (blue), $z = 50$ cm (orange), and $z = 100$ cm (green) lines. The solid lines represent the simulation results, and the dotted lines correspond to the theoretical calculations from Eq. (5).

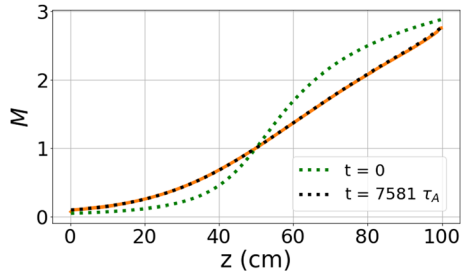

FIG. 8. Axial plasma velocity along the axis, for $r = 0$. The solid orange line is from simulations; the dotted green line is calculated using Eq. (5) with the original magnetic field from Eq. (13), and the dotted black line is calculated using Eq. (5) with the modified field from the simulations.

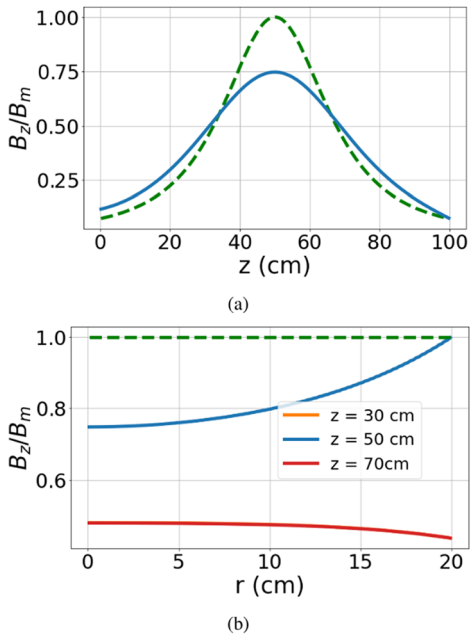

FIG. 9. (a) The axial profile of the B_z magnetic field at r = 0: green dashed line is the original field from Eq. (13), solid blue is the modified field from the simulations in the steady state. (b) The radial profile of the B_z at different z locations. The green dashed line is the original magnetic field line at $z = 50$ cm, the blue line is the modified magnetic at $z = 50$ cm. The profiles at $z = 30$ cm and $z = 70$ (the red and orange lines) overlap.

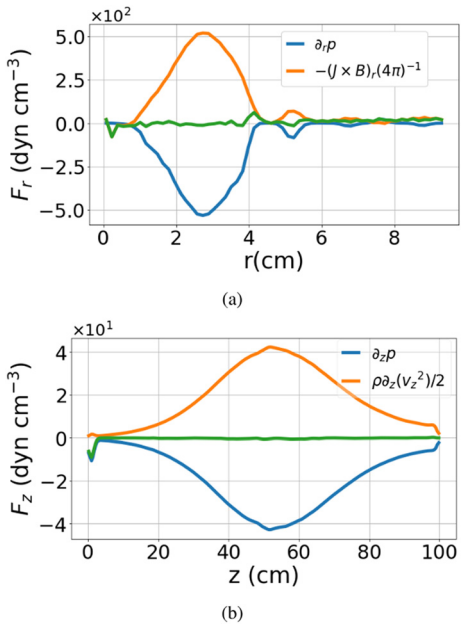

FIG. 10. The momentum balance for the main components in (a) the radial direction at z = 50 cm and (b) the axial direction at r = 0. (a) The sum of the pressure gradient and Lorentz forces is shown by the green line. (b) The sum of the pressure gradient and the axial inertial forces is shown by the green line. The other terms in the momentum balance are smaller at least by one order of magnitude, both for (a) and (b).

Figs. 9(a) and 9(b). Figure 9(a) shows that compared to the initial field, the axial profile of the B_z field in the stationary state at $t = 7581\tau_A$ becomes less peaked with a reduced amplitude at the maximum. The original magnetic field has a uniform profile radially, but the modified field is depressed in the radial direction toward the center; the value of B_z at the boundary remains the same, as shown in Fig. 9(b). The radial magnetic field has also changed. The numerical transonic profile, shown by the solid orange line in Fig. 8, shows excellent agreement with the analytical solution along the modified field near $r = 0$, as shown by the black dotted line at $t = 7581\tau_A$.

Initial magnetic field from Eq. (13) is not a true vacuum field since it has a finite (rather arbitrary) azimuthal current, $J_\theta = -r\partial B_z/\partial z$. In the final stationary state, the azimuthal plasma current is modified self-consistently to satisfy the force balance as shown in Figs. 10(a) and 10(b). Radially, the dominant terms are the radial pressure gradient balanced by the Lorentz force [Fig. 10(a)]. In the axial direction, the axial pressure gradient force is balanced by the inertial force due to the acceleration [Fig. 10(b)].

In this study, we extended the previous analytical results for the one-dimensional paraxial model to the full 2D $(r - z)$ geometry of the magnetic nozzle by performing full one-fluid ideal MHD simulations. We show here that the analytical solution obtained in Ref. 21 remains valid when applied to the arbitrary magnetic surfaces such that the plasma is transonically accelerated along the magnetic surfaces according to the analytical predictions from Eq. (5). Furthermore, we show here that within the full MHD model, the underlying magnetic field guiding the plasma is self-consistently modified to satisfy the momentum balance. In the radial direction, the primary balance is between the radial pressure gradient and the Lorentz force. In the axial direction, the primary balance describes the axial plasma acceleration by the axial pressure gradient force. In both directions, additional contributions from radial flows are small for our parameters.

It is important to note that the significant modification of the magnetic field observed in the case of a rather arbitrary magnetic field is not an effect of the finite plasma pressure. For our parameters, the plasma pressure parameter is rather small $\beta \simeq 1\%$. In some sense, the "self-healing" of the magnetic field is an artifact of the arbitrary magnetic field in the initial state, which was not current-free and, therefore, cannot represent the true vacuum field. In the presence of plasma, the MHD evolution (of the magnetic field, flow, and plasma pressure) drives the system toward a new equilibrium that (a) provides the thermal axial plasma acceleration in the magnetic nozzle conditioned by the converging–diverging magnetic field at the radial boundary; (b) satisfies the radial momentum balance, which is primarily the balance of the radial pressure gradient and the Lorentz force; and (c) plasma acceleration along the magnetic surface follows the earlier analytical predictions. We note that recent results[30] show that the plasma flow velocity measured in the plume of the magnetic nozzle of the electron cyclotron thruster is indeed in agreement with the theoretical predictions of Ref. 21. We have to note that the effects of plasma rotation, axial current, and the two-fluid (Hall) are not included in these simulations or the theoretical model.[21] The effects of plasma rotation and azimuthal magnetic field (due to the axial current) on plasma acceleration were considered in one-fluid MHD model in Ref. 31.

See the supplementary material for the evolution of the total energy in simulations and its saturation in the final state. The simulations were also repeated with higher resolution to confirm good convergence. While the stationary solutions studied in this paper are shown to be globally stable and robust, i.e., the rather arbitrary initial states converge to the unique transonic profile, on small scales we observe low amplitude fluctuations of the ion sound type propagating along the nozzle. The amplitude of such fluctuations is larger when the global solutions include the shock wave transitions at the nozzle inlet, as in some cases shown in Figs. 5 and 6. A dynamic visualization of the plasma velocity and density evolution is provided in the attached media, illustrating the transition to the transonic regime. This complements the static profiles shown in Figs. 3(a) and 3(b).

This work is supported in part by the Natural Sciences and Engineering Research Council of Canada (NSERC). The computational resources were provided by Digital Research Alliance of Canada.

AUTHOR DECLARATIONS

Conflict of Interest

The authors have no conflicts to disclose.

Author Contributions

N. Sheth: Data curation (lead); Formal analysis (lead); Investigation (lead); Methodology (equal); Visualization (lead); Writing – original draft (equal); Writing – review & editing (equal). **A. Smolyakov:** Conceptualization (lead); Formal analysis (lead); Funding acquisition (lead); Investigation (lead); Methodology (lead); Project administration (lead); Supervision (lead); Writing – original draft (lead); Writing – review & editing (equal). **J. Deguire:** Formal analysis (equal); Investigation (equal); Methodology (equal); Validation (equal); Writing – review & editing (supporting). **S. Pande:** Formal analysis (supporting); Investigation (supporting); Validation (supporting). **P. N. Yushmanov:** Conceptualization (equal); Formal analysis (equal); Investigation (equal).

DATA AVAILABILITY

The data that support the findings of this study are available from the corresponding author upon reasonable request.

REFERENCES

[1]A. V. Arefiev and B. N. Breizman, "Theoretical components of the VASIMR plasma propulsion concept," Phys. Plasmas **11**(5), 2942–2949 (2004).
[2]K. Wu, Z. Chen, J. Ren, Y. Wang, G. Zhang, W. Wang, and H. Tang, "A review of plasma acceleration and detachment mechanisms in propulsive magnetic nozzles," Phys. Plasmas **32**(4), 040501 (2025).
[3]M. Merino and E. Ahedo, "Fully magnetized plasma flow in a magnetic nozzle," Phys. Plasmas **23**(2), 023506 (2016).
[4]K. F. Schoenberg, R. A. Gerwin, R. W. Moses, J. T. Scheuer, and H. P. Wagner, "Magnetohydrodynamic flow physics of magnetically nozzled plasma accelerators with applications to advanced manufacturing," Phys. Plasmas **5**(5), 2090–2104 (1998).
[5]D. D. Ryutov, P. N. Yushmanov, D. C. Barnes, and S. V. Putvinski, "Divertor for a linear fusion device," AIP Conf. Proc. **1721**, 060003 (2016).
[6]D. Endrizzi, J. K. Anderson, M. Brown, J. Egedal, B. Geiger, R. W. Harvey, M. Ialovega, J. Kirch, E. Peterson, Y. V. Petrov, J. Pizzo, T. Qian, K. Sanwalka, O. Schmitz, J. Wallace, D. Yakovlev, M. Yu, and C. B. Forest, "Physics basis for the Wisconsin HTS axisymmetric mirror (WHAM)," J. Plasma Phys. **89**(5), 975890501 (2023).
[7]S. A. Andersen, "Continuous supersonic plasma wind tunnel," Phys. Fluids **12**(3), 557 (1969).
[8]K. Kuriki and O. Okada, "Experimental study of a plasma flow in a magnetic nozzle," Phys. Fluids **13**(9), 2262 (1970).
[9]S. N. Bathgate, M. M. Bilek, and D. R. McKenzie, "Electrodeless plasma thrusters for spacecraft: A review," Plasma Sci. Technol. **19**(8), 083001 (2017).
[10]M. Onofri, P. Yushmanov, S. Dettrick, D. Barnes, K. Hubbard, and T. Tajima, "Magnetohydrodynamic transport characterization of a field reversed configuration," Phys. Plasmas **24**(9), 092518 (2017).
[11]A. I. Morozov and L. S. Solovev, in *Steady-State Plasma Flow in a Magnetic Field*, Vol. 8 Reviews of Plasma Physics, edited by M. A. Leontovich (Springer US, New York, 1980).
[12]L. C. Steinhauer, "Formalism for multi-fluid equilibria with flow," Phys. Plasmas **6**(7), 2734–2741 (1999).
[13]E. Hameiri, "The equilibrium and stability of rotating plasmas," Phys. Fluids **26**(1), 230 (1983).
[14]L. Guazzotto and R. Betti, "Magnetohydrodynamics equilibria with toroidal and poloidal flow," Phys. Plasmas **12**(5), 056107 (2005).
[15]J. P. Goedbloed, "Transonic magnetohydrodynamic flows in laboratory and astrophysical plasmas," Phys. Scr. **T98**, 43–47 (2001).
[16]M. Velli, "Hydrodynamics of the solar wind expansion—Why is the solar wind supersonic?," Astrophys. Space Sci. **277**(1–2), 157–167 (2001).
[17]K. Tsinganos, *Theory of MHD Jets and Outflows*, Vol. 723 Lecture Notes in Physics (Springer Berlin Heidelberg, 2007), pp. 117–159.
[18]A. Fruchtman, K. Takahashi, C. Charles, and R. W. Boswell, "A magnetic nozzle calculation of the force on a plasma," Phys. Plasmas **19**(3), 033507 (2012).
[19]T. Lafleur, "Helicon plasma thruster discharge model," Phys. Plasmas **21**(4), 043507 (2014).
[20]W. M. Manheimer and R. F. Fernsler, "Plasma acceleration by area expansion," IEEE Trans. Plasma Sci. **29**(1), 75–84 (2001).
[21]A. I. Smolyakov, A. Sabo, P. Yushmanov, and S. Putvinskii, "On quasineutral plasma flow in the magnetic nozzle," Phys. Plasmas **28**(6), 060701 (2021).
[22]A. E. Dubinov and I. D. Dubinova, "How can one solve exactly some problems in plasma theory," J. Plasma Phys. **71**(05), 715 (2005).
[23]R. M. Corless, G. H. Gonnet, D. E. G. Hare, D. J. Jeffrey, and D. E. Knuth, "On the LambertW function," Adv. Comput. Math. **5**(1), 329–359 (1996).
[24]M. Jimenez, A. I. Smolyakov, O. Chapurin, and P. Yushmanov, "Ion kinetic effects and instabilities in the plasma flow in the magnetic mirror," Phys. Plasmas **29**(11), 112117 (2022).
[25]A. Sabo, A. I. Smolyakov, P. Yushmanov, and S. Putvinski, "Ion temperature effects on plasma flow in the magnetic mirror configuration," Phys. Plasmas **29**(5), 052507 (2022).
[26]M. Tyushev, A. Smolyakov, A. Sabo, R. Groenewald, A. Necas, and P. Yushmanov, "Drift-kinetic PIC simulations of plasma flow and energy transport in the magnetic mirror configuration," Phys. Plasmas **32**(3), 032514 (2025).
[27]J. Deguire, "Plasma flow and acceleration in the magnetic mirror and nozzle geometries," M.Sc. thesis (University of Saskatchewan, 2024), https://hdl.handle.net/10388/16446.
[28]R. F. Post, "The magnetic mirror approach to fusion," Nucl. Fusion **27**(10), 1579–1739 (1987).
[29]A. Mignone, G. Bodo, S. Massaglia, T. Matsakos, O. Tesileanu, C. Zanni, and A. Ferrari, "PLUTO: A numerical code for computational astrophysics," Astrophys. J. Suppl. **70**(1), 228–242 (2007).
[30]R. Pioch, "Ion dynamics in the magnetic nozzle of an electron cyclotron resonance Thruster—Dynamiques ioniques dans la tuyère magnétique d'un propulseur ECR," Ph.D. thesis (Institut Polytechnique de Paris, 2025). https://theses.hal.science/tel-04861648.
[31]A. I. Smolyakov, A. Sabo, S. Krasheninnikov, and P. Yushmanov, "Electromagnetic and centrifugal effects on plasma acceleration in the magnetic nozzle," Plasma Phys. Rep. **51**, 427 (2025).